

# Growth and anisotropy of ionization fronts near high redshift quasars in the MassiveBlack simulation

Yu Feng<sup>1\*</sup>, Rupert A.C. Croft<sup>1</sup>, Tiziana Di Matteo, and Nishikanta Khandai

<sup>1</sup>*McWilliams Center for Cosmology, Department of Physics, Carnegie Mellon University, Pittsburgh, PA 150213*

December 7, 2022

## ABSTRACT

We use radiative transfer to study the growth of ionized regions around the brightest,  $z=8$  quasars in a large cosmological hydrodynamic simulation that includes black hole growth and feedback (the MassiveBlack simulation). We find that in the presence of the quasar the comoving HII bubble radii reach 10 Mpc/h after 20 My while with the stellar component alone the HII bubbles are smaller by at least an order of magnitude. Our calculations show that several features are not captured within an analytical growth model of Stromgren spheres. The X-ray photons from hard quasar spectra drive a smooth transition from fully neutral to partially neutral in the ionization front. However the transition from partially neutral to fully ionized is significantly more complex. We measure the distance to the edge of bubbles as a function of angle and use the standard deviation of these distances as a diagnostic of the isotropy of ionized regions. We find that the overlapping of nearby ionized regions from clustered halos not only increases the anisotropy, but also is the main mechanism which allows the outer radius to grow. We therefore predict that quasar ionized bubbles at this early stage in the reionization process should be both significantly larger and more irregularly shaped than bubbles around star forming galaxies. Before the star formation rate increases and the Universe fully reionizes, quasar bubbles will form the most striking and recognizable features in 21cm maps.

**Key words:** Stromgren sphere – quasar – cosmology – simulation

## 1 INTRODUCTION

The current consensus is that the contribution to the global ionizing budget from quasars during the Epoch of Reionization (EOR) is small compared to that from early stars and galaxies (see, eg, Loeb 2009; Giroux & Shapiro 1996; Trac & Gnedin 2011). The characteristic proper radius of ionizing bubbles at the end of EoR is constrained to be on the order of 10 Mpc/h (Wyithe & Loeb 2004), and the quasar contribution is limited to be less than 14% (Srbnovsky & Wyithe 2007) of the total. Even though the contribution to global reionization by quasars is constrained in this way, bright quasars may still leave a signature on the growth of individual ionized regions. Several authors have investigated this signature in mock 21cm emission spectra taken from simulations of isolated quasars (Majumdar et al. 2011; Datta et al. 2008; Geil & Wyithe 2008). In observations, an object recently reported by Mortlock et al. (2011), ULAS J1120+0641, has a luminosity of  $6.3 \times 10^{13} L_{\odot}$  at  $z \sim 7$  and a proper near-zone radius of less than 2 Mpc/h. The near-zone radius is consistent with the possibility of bright quasar

driven growth in a near neutral IGM background (Bolton et al. 2011).

In this paper we study the growth of the ionization front of bright quasars in an almost neutral cosmological context. The quasars and their surrounding medium are selected from a large hydrodynamic simulation (the MassiveBlack simulation, introduced in Di Matteo et al. (2012)), and then post-processed with a radiative transfer code. This allows us to simulate 8 rare quasars using reasonable computing resources. Our focus is on the evolution and properties of the largest individual ionized bubbles, the sources that produce them, and the relationship between the two. Because the simulation forms quasars and star forming galaxies ab initio, we are able to make use of the luminosities and positions of the radiation sources that the simulation produces, rather than setting them in by hand. In this paper, however we do not deal with the full reionization of the volume of the simulation, which would require following the evolution of the entire density and ionization field from high redshifts down to at least  $z = 6$ . Instead we restrict ourselves to the growth of ionized regions around an early period in this process (at  $z = 8$ ), where the photon path lengths are still smaller than the computational subvolumes we analyze. We

\* yfeng1@cmu.edu

leave the study of the full reionization of the volume to future work.

## 2 HYDRODYNAMIC SIMULATION

The SPH output we use is from the MassiveBlack simulation (see Di Matteo et al. (2012); DeGraf et al. (2012); Khandai et al. (2012) for further details), which was run with a  $\Lambda$ CDM cosmology with parameters  $(\Omega_\Lambda, \Omega_M, \Omega_b, h, \sigma_8) = (0.74, 0.26, 0.044, 0.72, 0.8)$ . A total number of  $2 \times 3200^3$  gas and dark matter particles were followed in a box of  $0.75 \text{ Gpc}^3$  from red-shift  $z = 159$  to red-shift  $z = 4.75$ . This simulation is by far the largest cosmological hydrodynamics simulation run with the P-GADGET 3 program.

This run not only contains gravity and hydrodynamics but also all the extra physics (subgrid modeling) for star formation (Springel & Hernquist 2003), black holes and associated feedback processes.

The basics aspects of our black hole accretion and feedback model (Di Matteo et al. 2008) consist of representing black holes by collisionless particles that grow in mass (from an initial seed black hole) by accreting gas in their environments. The accretion rate is given by

$$\dot{M} = \min(M_{\text{Bondi}}, M_{\text{Edd}}), \quad (1)$$

and

$$\dot{M}_{\text{Bondi}} = \frac{4\pi G^2 M_{\text{BH}}^2 \rho}{(c_s^2 + v^2)^{3/2}}, \quad (2)$$

where  $\rho$  and  $c_s$  are the density and sound speed of the ISM gas respectively, and  $v$  is the velocity of the black hole relative to the gas, and  $\dot{M}_{\text{Edd}} = L_{\text{Edd}}/(\eta c^2)$  (where  $L_{\text{Edd}}$  is the BH Eddington Luminosity,  $L_{\text{Edd}} = 1.26 \times 10^{38} \text{ ergs}^{-1}$ ). At the high redshift and high halo masses we are carrying out the analysis here, black holes are accreting at their Eddington rates (DeGraf et al. 2012) making any detail of the subgrid models for black holes virtually irrelevant.

For the black hole feedback, a fraction of the radiative energy released by the accreted material is assumed to couple thermally to nearby gas and influence its motion and thermodynamic state (typically referred as BH feedback). The radiated luminosity,  $L_r$ , from the black hole is related to accretion rate,  $\dot{M}_{\text{BH}}$ , as

$$L_{\text{bol}} = \eta (\dot{M}_{\text{BH}} \times c^2), \quad (3)$$

where we take the standard mean value  $\eta = 0.1$ . Some coupling between the liberated luminosity and the surrounding gas is expected: in the simulation 5% of the luminosity is (isotropically) deposited as thermal energy in the local black hole kernel, providing some form of feedback energy. With our simulations the activity of quasars is directly derived from the accretion history. The luminosity of the stars and galaxies can be derived from the star formation rate history which is provided by the multiphase star formation model in the simulation (Springel & Hernquist 2003). The multiphase star formation model also provides a mechanism to remove the self-shielded interstellar medium (ISM) from the matter density field.

#H	#V	$M_{\text{HALO}}$	$M_{\text{BH}}$	Total		Center	
				QSO	STR	QSO	STR
0	0	148.35	74.6	8.35	3.38	7.24	0.94
1	1	77.9	49.6	4.97	3.45	4.43	0.79
2	2	75.5	34.7	2.06	3.93	1.39	0.45
3	0	84.9	7.3	8.35	3.71	0.49	0.22
4	3	60.1	119.0	8.18	2.72	7.76	0.54
5	0	67.1	16.0	8.35	3.71	0.56	0.21
6	4	70.8	5.5	0.50	2.72	0.06	0.16
7	5	65.6	13.2	0.95	1.98	0.69	0.30
8	6	66.6	6.4	1.29	3.82	0.20	0.21
9	7	64.9	7.2	0.38	2.22	0.15	0.15

**Table 1.** UV Flux of Subvolumes. The first column #H (0 - 9) identifies the ten most massive halos. The second column #V (0 - 7) identifies the eight unique subvolumes that contain the halos. The halo mass ( $M_{\text{HALO}}$ ) is in units of  $10^{10} M_\odot h^{-1}$ . The blackhole mass ( $M_{\text{BH}}$ ) is in units of  $10^6 M_\odot h^{-1}$ . The luminosities are in units of  $10^{55} \text{ sec}^{-1}$ . Halos 0, 3, and 5 are clustered and belong to the same subvolume 0.

## 3 $Z = 8$ QUASARS IN MASSIVEBLACK

The Epoch of Reionization (EoR) is currently constrained to be between  $z = 10$ , by the CMB measurement (Komatsu et al. 2009), and  $z = 6$ , by the Sloan Digital Sky Survey measurements of the intergalactic medium surrounding high redshift quasars (Fan et al. 2006; Willott et al. 2007). During the MassiveBlack run, a uniform UV background radiation field is introduced at the end of the EoR in the optically thin approximation (see e.g. Bolton & Haehnelt (2007)). At  $z = 8$  the uniform radiation has not yet been switched on, so that IGM surrounding quasars is mostly fully neutral. In a postprocessing step (see below), we then model the radiation field with radiative transfer, using both a full spectrum quasar component for black hole sources and a UV spectrum stellar component for the stellar sources.

In MassiveBlack, the quasars are rapidly accreting supermassive black holes, and their fuelling is driven from the large scales and occurs through high density cold flows along the cosmic filaments Di Matteo et al. (2012). In general larger halos host brighter quasars unless (i) the quasar is turned off by feedback, or (ii) the quasar has not yet grown its black hole mass significantly. We select a quasar system based on halo mass, taking the 10 most massive halos in the simulation at redshift  $z = 8$  (see Table 3). For each of the halos, we cut a cubical subvolume of side length  $50 \text{ Mpc}/h$  from the original simulation. Due to their clustering, three of the halos (halo number 0, 3 and 5 in Table 3) form at spatial locations within subvolume 0. Only 8 unique subvolumes are identified, which we refer as subvolume 0 to 7 throughout the rest of the paper.

Next, we compute the luminosity due to the quasars and star formation occurring in each of the subvolumes. The assignments of luminosities are described in sections 3.1 and 3.2. We show the total UV flux of all sources in the region and that of the central sources within the  $1 \text{ Mpc}/h$  radius of the center in Table 1 and Figure 1. There is an expected

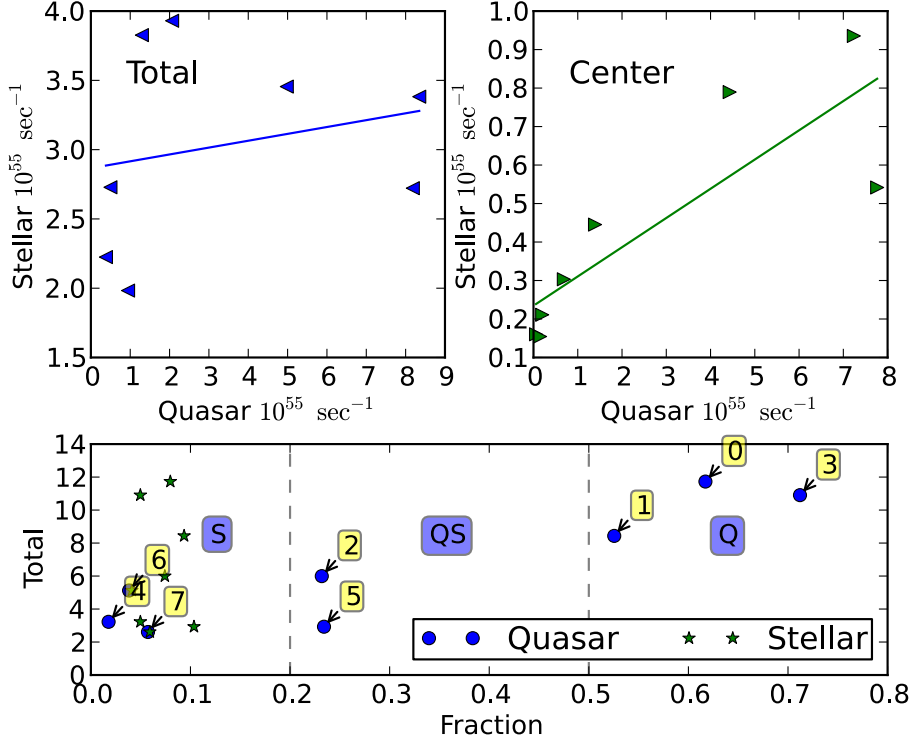


**Figure 1.** Sample Luminosity. The left panel compares the total UV photon luminosities of the stars and the quasars within the subvolumes. The right panel compares the UV photon luminosities from the sources within 1 Mpc/h of the center. The central sources directly contribute to the growth of the central ionized region (CIR). The dotted lines represent the linear regression of the data. In the bottom panel the central luminosity as a fraction of the total luminosity is shown. The subvolumes fall into three categories: (S) Stellar Driven, (QS) Subdominant Quasar, (Q) Quasar Driven.

correlation between the central quasar and central stellar luminosity. Based on the ratio of the central luminosity to total ionizing luminosity within the subvolume, as well as the composition (quasar or stellar) of the central luminosity, we can divide the subvolumes into three groups:

- **Stellar (S):** The quasar luminosity in the central sources is smaller than the sum of stellar luminosities, and the entire central source luminosity is small comparing to the ionizing luminosity of the entire box. We note there can be two possible distributions of sources within the box: one being the presence of another major source that is not near the center of the subvolume; the other being ionizing sources that are rather more uniformly distributed throughout the subvolume. In our subvolumes, the latter is more often to the case.
- **Subdominant Quasar (QS):** The central quasar luminosity dominates the central luminosity, but is not a significant fraction of the total luminosity of sources in the subvolume.
- **Quasar (Q):** The central quasar luminosity dominates the entire subvolume.

### 3.1 Quasar Radiation

We calculate the bolometric luminosity  $L_{\text{bol}}$  of each quasar from the accretion rate  $\dot{M}$  of the supermassive black hole with equation (3). We choose to use as  $\dot{M}$  a single value

Band	Range
UV	13.6 eV to 250 eV
Soft X-Ray	250 eV to 2 KeV
Hard X-Ray	2 eV to 10 KeV

**Table 2.** Band definitions.

throughout the calculation, which is averaged accretion rate measured from the simulation over a timescale  $t_Q = 2 \times 10^7$  yrs, where  $t_Q$  is also the length of time over which we follow the evolution of the quasar ionization front. We estimate the luminosities in different bands from the bolometric luminosity according to the fitting formula of Hopkins et al. (2007). The band definitions are listed in Table 2. The luminosity in UV band is estimated from B band luminosity, assuming power laws with optical index of  $\alpha_{\text{UV}} = 1.76$  and  $\alpha_B = 0.44$  respectively,

$$L_{\text{uv}} = \frac{L_B}{\nu_B} \left( \frac{\nu_X}{\nu_B} \right)^{-\alpha_B} \left( \frac{\nu_I}{\nu_X} \right)^{-\alpha_{\text{UV}}} \frac{\left( \frac{250}{13.6} \right)^{1-\alpha_{\text{UV}}} - 1}{1 - \alpha_{\text{UV}}}, \quad (4)$$

where  $\nu_X = c/120 \text{ nm}$  is the pivot from optical to UV,  $\nu_B = c/445 \text{ nm}$  and  $\nu_I = c/91.1 \text{ nm}$ . We calculate the photon flux of the quasar sources according to these power law spectra applied to the various bands.

### 3.2 Stellar Radiation

The stellar luminosity of a halo is given by

$$\dot{N}_{\text{SFR}} = f_{\text{esc}} N_{\gamma/b} X_H \Phi / m_p, \quad (5)$$

where  $\Phi$  is the star formation rate of the halo,  $X_H = 0.76$ , and  $m_p$  is the proton mass. We take the escape fraction to be  $f_{\text{esc}} = 0.1$ , and the photon to baryon ratio to be  $N_{\gamma/b} = 4000$ , a value found to produce a reionization history consistent with observations by Furlanetto et al. (2004); Sokasian et al. (2003). For simplicity, the stellar sources are assigned to the center of the halo; in future work we plan to investigate the effect of the positioning of the stellar sources by either following the star forming gas particles in the simulation directly or the gravitationally bound subhalos. To ease the modelling, we only include and assume the same UV band spectrum for the stellar radiation to that of the Quasar spectrum.

## 4 ANALYTIC GROWTH OF STROMGREN SPHERES

The growth of Stromgren spheres in a clumpy cosmological environment can be analytically modeled using (Cen & Haiman 2000),

$$\frac{dR_t^3}{dt} = 3H(z)R_t^3 + \frac{3\dot{N}_{\text{ph}}}{4\pi \langle n_H \rangle} - C_H \langle n_H \rangle \alpha_B R_t^3, \quad (6)$$

where the first term represents the Hubble expansion, and can be neglected in the current context. The solution is straightforward (eg, Majumdar et al. 2011)

$$\begin{aligned} R_t &= R_s \left( 1 - \exp\left(-\frac{t}{t_s}\right) \right)^{-1/3} \approx R_s \cdot \left( \frac{t}{t_s} \right)^{1/3} \\ t_s &= (C_H \langle n_H \rangle \alpha_B)^{-1} \\ R_s &= \left( \frac{3\dot{N}_{\text{ph}}}{4\pi C_H \langle n_H \rangle^2 \alpha_B} \right)^{1/3}. \end{aligned} \quad (7)$$

We use this analytic solution to compare to our numerical results, but first we need to measure the constants in the above expression from the simulation subvolumes. We calculate the clumping factor  $C_H$  using a method appropriate for an SPH simulation, described by Pawlik et al. (2009),

$$C_H = \frac{\sum \rho_i^2 h_i^3}{\langle \rho \rangle^2 \sum h_i^3}, \quad (8)$$

where  $h_i$  is the SPH smoothing length. The clumping factor we measure from the gas in the entire subvolumes has a value  $C_H \sim 4$ , giving a recombination time about  $t_s \sim 100 \text{ myear} \gg t_Q$ . However we note the clumping factor can go up to  $\sim 20$  within 1 Mpc/h radius from the center of the subvolume, reducing  $t_s$  to  $\sim 20 \text{ myear}$ . For the values of  $\rho_i$ , we use the density of the intergalactic medium (IGM) gas component which is relevant to the radiative transfer: the interstellar medium (ISM) is excluded in consistency with the simulation; see below.

For the source luminosity, we make the simplest approximation, summing the luminosities of all sources within the subvolume to obtain one effective  $\dot{N}_{\text{ph}}$ . We also assume that the volume consists of pure hydrogen ( $X_H = 1$ , i.e. no helium) in the calculation of the analytic model. The recombination rate  $\alpha_B$  is taken from Hui & Gnedin (1997).

## 5 RADIATIVE TRANSFER SIMULATION

For this study we have rewritten the SPHray Monte Carlo radiative transfer code (Altay et al. 2008; Croft & Altay 2008) in C with OpenMP(TM), so that it runs in parallel on shared memory systems. We have also eliminated the on-the-spot approximation of recombination, so that instead recombination rays are emitted when the recombination photon deposit at a spot exceeds a threshold, as done in the code CRASH (Maselli et al. 2003). The parallel version allows us to trace many rays at the same time on several CPUs within a single time step, achieving a near-linear speed up with a small number ( $10 \sim 30$ ) of CPUs. Monochromatic rays are sampled from frequency space according to the source spectrum. Hydrogen and Helium ionization and recombination are both traced. The tabulated atomic reaction rates of Hui & Gnedin (1997) taken from the serial version SPHray are used.

As a new addition to the code we model the secondary ionization of high energy photons using a fit to the Monte Carlo simulation results of Furlanetto & Stoever (2010); Shull & van Steenberg (1985). These fast non-thermal-equilibrium electrons produced from high energy ionization photons (e.g., X-ray photons) may collide and secondarily ionize more neutral atoms, increasing the ionizing efficiency of the quasar sources by allowing one high energy photon to ionize tens of neutral atoms. On the other hand, our current post processing approach is incapable of modeling the heating from the residual energy of the ionizing photons, because in this approach the thermal evolution is decoupled from radiative transfer. MassiveBlack contains a calibrated thermal term in the black hole feedback mechanism, which addresses this issue, at the expense of injecting the heating energy only locally to the vicinity of the black hole.

The inter-stellar medium (ISM) component of gas particles condenses into cold clouds which are self-shielded from cosmic radiative transfer (except that they may host stellar radiative sources). As a result we excise them from the matter density field when performing the ray tracing calculation (by doing this we also assume that their small cross-section would not have affected ray tracing for the rest of the gas). MassiveBlack has a multiphase (cold, hot gas phases) star formation model, from which we identify the cold cloud component with the ISM (Springel & Hernquist 2003). The cold fraction is an increasing function of the mean density of the gas particle, effectively removing the densest particles from the density field in a manner similar to the threshold method used to calculate the clumping factor by Pawlik et al. (2009), and, the removal of the cold high density gas in the X-ray emission calculation by Croft et al. (2001).

In MassiveBlack the total (IGM + ISM) mean baryon density around quasar sources can be as high as  $60 \text{ cm}^{-3}$ . Were the ISM not removed from the ray tracing, the high mean density would shield off the radiation and prevent the growth of any cosmic scale ionized regions. Figure 2 shows the histogram of the overdensity of gas particles before and after the removal of cold clouds in one of the subvolumes.

### 5.1 Parameterizing the Ionization Front

We use the center of the chosen halo to define the center of the subvolume, and also the central ionized region (CIR).

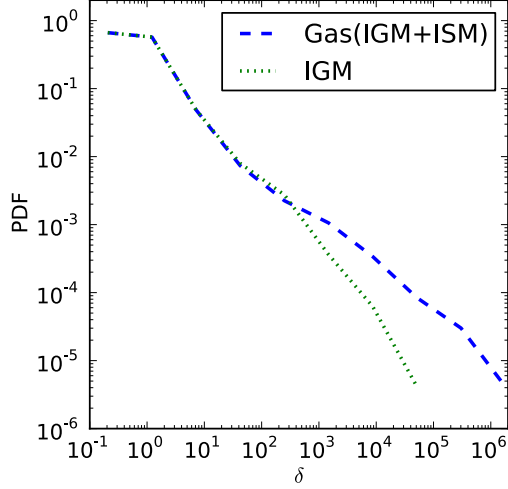


**Figure 2.** IGM density and total gas density histogram. The dashed line is the total gas density, while the dotted line is the IGM density. The histogram is performed on the overdensity of the particles in the simulation. Using the IGM density results a reduction in the number of dense particles and allows a sensible treatment of the radiation transfer.

When quantifying the size of the CIR we measure the spherically averaged fraction in a species,  $x$  using (we show the example of HII regions, similar definitions hold for other species):

$$x_{\text{HI}}(r) = \frac{\int \delta(r' - r) x_{\text{HI}} \rho dV}{\int \delta(r' - r) \rho dV} \doteq \frac{\sum_{\text{shell}} x_{\text{HI},i} m_i}{\sum_{\text{shell}} m_i}, \quad (9)$$

Here the sums are carried out by binning SPH particles (index  $i$ ) in shells. Particles are assigned as a whole to shells by their center position rather than being integrated over the SPH kernel within the shell. We define the averaged CIR radius at a given threshold  $x^*$  to be the first crossing of  $x(r)$  with  $x^*$ , or

$$\hat{R}_S(x) = \inf\{r | x_{\text{HI}}(r) = x^*\}. \quad (10)$$

The first crossing corresponds to the edge of the CIR, and later crossings indicate the edges of the nearby ionized regions. The motivation for this definition comes from its similarity to that used to quantify ionized regions seen in quasar absorption line spectra, the Ly $\alpha$  absorption Near-Zone radius  $R_{\text{NZ}}$  by Fan et al. (2006). In practice, we take as  $\hat{R}_S$  the average of the two nearest bins  $r_L$  and  $r_R$  which satisfy  $[x_{\text{HI}}(r_L) - x][x_{\text{HI}}(r_R) - x] < 0$ .

The spherically averaged radius  $\hat{R}_S$  is a simple quantity to use in comparisons but the angular variations in the properties of the CIR are completely lost. To quantify the angular dependency, we bin the SPH particles into angular cones and calculate the averaged fraction within the cones,

$$x_{\text{HI}}(r, \theta, \phi) \doteq \frac{\sum_{\text{cone, shell}} x_{\text{HI},i} m_i}{\sum_{\text{cone, shell}} m_i}. \quad (11)$$

The angular dependent CIR radius is

$$R_s(x, \theta, \phi) = \inf\{r | x_{\text{HI}}(r, \theta, \phi) = x^*\}. \quad (12)$$

Note that in general  $\langle R_s(x, \theta, \phi) \rangle \neq \hat{R}_S$ , because averaging and binning do not commute. For measuring  $R_s(x, \theta, \phi)$ ,

we use  $12 \times 16^2$  cones. We note that increasing to  $12 \times 32^2$  cones does not significantly alter the results.

We measure the anisotropy of the ionized bubble from the variance of  $R_s$

$$A_s(x) = ST_k[R_s(x, \theta_k, \phi_k)], \quad (13)$$

where  $ST_k$  stands for the standard deviation. We run the simulation with sufficient number of rays so that the typical shot noise contribution towards  $A_s$  is negligible, as shown in the next section.

Three different levels of species fraction  $x$  are used to define three different levels of CIR fronts in this study:

- i Inner front,  $x = 0.1$  for the neutral fraction, or  $x = 0.9$  for the ionized fraction;
- ii Middle front,  $x = 0.5$  for the neutral fraction;
- iii Outer front,  $x = 0.9$  for the neutral fraction, or  $x = 0.1$  for the ionized fraction.

The Inner front corresponds to the near-ionized edge of the Stromgren sphere, and the Outer front corresponds to the near-neutral edge of the Stromgren sphere. We however note that these choices are for illustrative purposes only and they do not have any direct correspondence with threshold values used to detect 21 cm or Ly $\alpha$  observation signatures.

## 5.2 Shot-noise and Convergence

One issue which must be addressed in Monte Carlo ray tracing (RT) schemes is the presence of shot noise and its effect on convergence of results, something particularly important when sampling is also in frequency space (eg Iliev et al. 2006, on CRASH). Shot noise artificially increases the angular anisotropy  $A_s$  measure, and so is of direct concern for this study.

We define a shot noise parameter  $\gamma$  to be the ratio between the number of photons in a ray packet,  $n_r^0$  and the number of atoms in an SPH particle  $n_p^0$ ,

$$\gamma = \frac{n_r^0}{n_p^0}. \quad (14)$$

A small  $\gamma$  guarantees that the ionization front cannot advance by more than one particle in one time step. When  $\gamma \ll 1$ , the ionization front advances slowly and the shot noise is controlled. One of course still needs to ensure the rays have a sufficient angular resolution to resolve the angular scale used in the calculation of the anisotropy.

In MassiveBlack, a typical SPH gas particle has a mass of  $5 \times 10^7 M_\odot/h$ , equivalent to  $n_p^0 = 9 \times 10^{64}$ . For ray tracing with  $10^5$  steps and 128 rays per time step, ( $1.28 \times 10^7$  rays), and with the total luminosity listed in Table 1, an average packet contains  $n_r^0 = 3 \times 10^{63}$  photons. The shot noise parameter is therefore  $\gamma = 0.03 \ll 1$  for our typical runs.

We can also empirically confirm that convergence is reached by increasing the number of rays used in the simulation and showing that the quantity of interest is insensitive to further increases. We perform such a convergence test with 3 runs on subvolume 4 with (i)  $1.3 \times 10^8$  rays,  $\gamma = 0.003$ , (ii)  $1.3 \times 10^7$  rays,  $\gamma = 0.03$ , and (iii)  $1.3 \times 10^6$  rays,  $\gamma = 0.3$ . We quantify the similarity of the ionization front using the correlation coefficient of  $R_s(\theta, \phi)$  between runs, shown in Table 3. The higher correlation between the runs with more

Runs	HII Inner	HII Middle	HII Outer
0.003 and 0.03	0.96	0.98	0.86
0.03 and 0.3	0.74	0.94	0.68

**Table 3.** Correlation Coefficients. Shown in the table are the correlation coefficient of the center bubble radius  $R_s(\theta, \phi)$  between different runs.

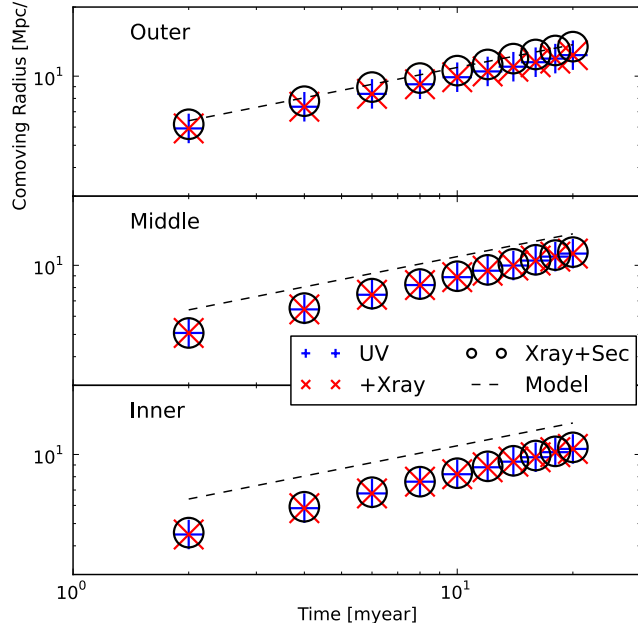


**Figure 3.** CIR Growth in a Uniform Density Field. The symbols are: (i) cross[+]: UV only; (ii) cross[x]: UV and X-ray (iii) circle: UV and X-ray, with Secondary ionization. The analytic model (dashed lines) neglects Helium and assumes  $X_H = 1.0$ .

rays indicates that the simulation has effectively converged.

## 6 RESULTS AND DISCUSSION

### 6.1 Uniform Density Field

We first test P-SPHRAY with a source in a uniform density field at  $z = 8$ , with H number density  $n_H = 2 \times 10^{-4} \text{ cm}^{-3}$ , and uniform temperature  $T = 10^4 \text{ K}$ . The hydrogen mass fraction is  $X_H = 0.76$ , the cubical box has a side length of 50 Mpc/h, and we evolve the radiation and ionization fractions for a duration of  $2 \times 10^7 \text{ yrs}$ . We carry out 3 separate simulations, considering different central source properties for each one as follows: (i)  $1.2 \times 10^{56} \text{ sec}^{-1}$  UV; (ii)  $1.2 \times 10^{56} \text{ sec}^{-1}$  UV,  $0.3 \times 10^{55} \text{ sec}^{-1}$  soft X-Ray,  $0.5 \times 10^{55} \text{ sec}^{-1}$  hard X-Ray; (iii) same as (ii), with secondary ionizations. The luminosity of the source is motivated by the luminosity of the center sources in subvolume 0. The growth of the CIR fronts in the simulations are shown as a function of time in Figure 3. We show as separate panels the behaviours of the three parts of the ionization front: inner, middle and outer (as defined in section 5.1).

There are two highlights from the uniform density field simulations: (i) The outer front agrees well with the free

streaming power law with an index of  $1/3$  in equation (7). The inner and middle fronts are smaller than the analytic model due to a lower ionization threshold used to define the front. (ii) The effect of X-ray photon and secondary ionizations is quite limited on the inner and middle front. The effect is more evident on growth of the outer front. This is because the secondary ionizations affect the way the harder photons interact with the matter the most, and harder photons travel further into the neutral region. We note that by adding in the effect of secondary ionizations increases the outer radius of ionized bubbles by approximately 10%.

### 6.2 MassiveBlack: Visualization

We show the CIR bubble of the most extreme Q type and S type subvolumes (subvolume number 3 and 4 in Table 3 respectively) in Figure 4. The halo mass of both are similar,  $60 \times 10^{10} M_\odot h^{-1}$  and so are their total star formation rates. However subvolume 3 has a large ionized HII region associated with the bright active quasar in the center of the subvolume, whilst in subvolume 4 the HII region formed merely from stellar sources are small. Note that, even though of comparable mass halo, the central black hole is much smaller in subvolume 3 and hence its activity has a negligible impact. This example aims to illustrate how, in the presence of an active early quasar, the ionized bubble is far more extensive than one driven by star formation alone.

The time evolution of the HII bubble in subvolume 0, where three halos coexist, is shown graphically with a slice through the center of the simulation volume every  $2 \times 10^6 \text{ yr}$  in Figure 5. It is interesting to observe that a neighbouring bubble on the right merges with the center bubble and this increases the size of the outer front in that direction, contributing to the anisotropy of the front. We investigate this issue in the next section in a more quantitative way.

### 6.3 MassiveBlack: Spherically Averaged Radius of Ionized Regions

We now examine the results of the radiative transfer post-processing of the eight subvolumes from MassiveBlack. The averaged CIR radius  $\bar{R}_s$  for HII and HeIII, as defined in section 5.1, are shown in Figure 6 as functions of the central source flux. We also plot fits of the growth to the  $1/3$  free streaming power law (7). At the low luminosity end (mainly S type and QS type subvolumes) there is a significant deviation from the fit for the inner and middle fronts. The outer front is more extended than the simple uniform field simulation, although the source spectra are similar, hinting that the structure in the IGM is also contributing to the smoothing of the front. This smoothing is a phenomenon similar to that described by Wyithe & Loeb (2007). We also attribute the effect to the clustering of sources; however unlike the smoothing due to secondary ionization, the clustering contribution is anisotropic, and we discuss it in section 6.4.

In Figure 6, we can see that the HII and HeII CIR radii appear to grow together. The correlation between the two can be seen directly by plotting one against the other, which we do in Figure 7, where we find there is a strong correlation between the HII radius and HeIII radius. The HeIII radius is smaller than the HII radius, agreeing with the finding of



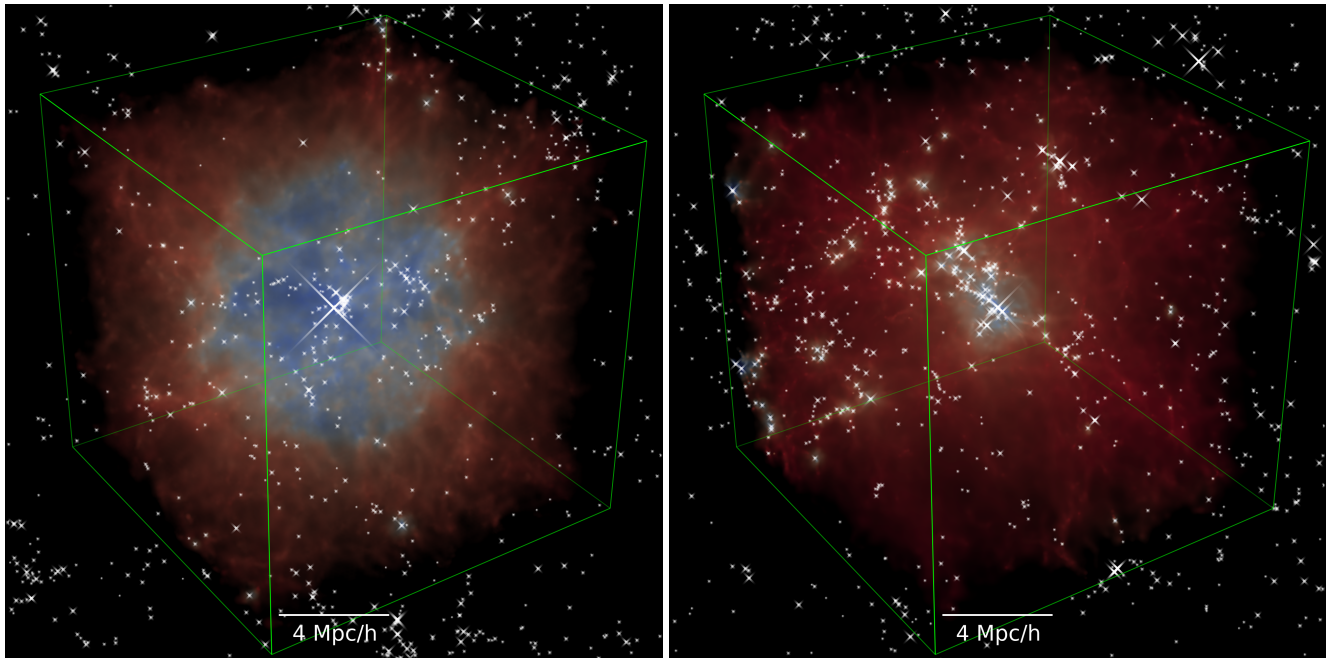


**Figure 4.** Q (Quasar, left) type and S (Stellar, right) type ionized bubbles in MassiveBlack. Both panels are of comoving length 15 Mpc/h per side. A camera is put at about 60 Mpc/h from the center of the subvolume and a perspective transformation is applied to form a projection onto the image plane of the camera. Red color corresponds to fully neutral IGM and blue color corresponds to fully ionized IGM. Yellow is in between two states. Crosses are the sources; both stellar and quasar sources of the entire subvolume are shown. It is interesting to notice the lack of a major source (comparing to the bright quasar in subvolume 3) in subvolume 4.

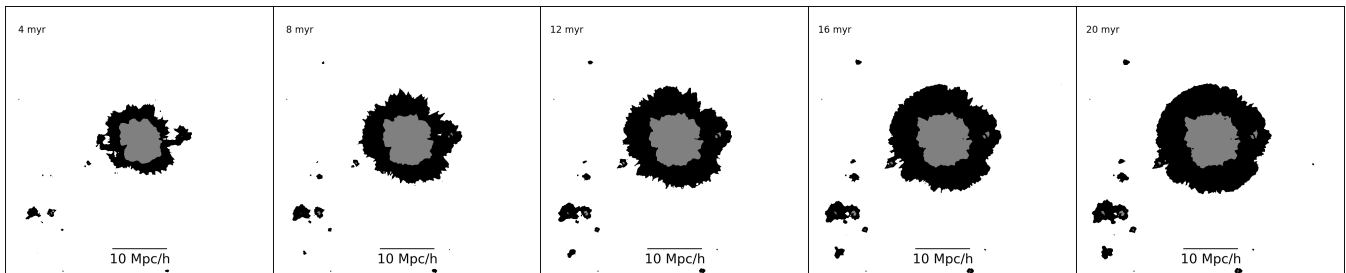


**Figure 5.** Evolution of the ionization front. The evolution of the ionization front in subvolume #0 is shown. The ionization front ( $x_{\text{HI}} \in [0.1, 0.9]$ ) is marked in black, and the fully ionized near zone ( $x_{\text{HI}} < 0.1$ ) is marked with gray.

Friedrich et al. (2012) who used the ray tracing code C2Ray. We note however that the treatment of secondary ionization and Helium ionization in P-SPHRAy is similar to that of C2Ray, and an agreement is not surprising.

The time evolution history of the HII CIR radius for all subvolumes is shown in Figure 8. We compare the evolution of the three parts of the fronts with the prediction of the analytic model (in equation 7), in which we have used the clumping factor and mean H density measured within the final CIR in the simulation to estimate a fiducial recombination time  $t_S$ .

The growth of the CIR in the Q type subvolumes flattens off much earlier than one might expect from a free streaming law. In order to ascertain the relevant physical timescales, we fit the time evolution of the fronts to the full analytic model in equation (7), and extract the effective recombination time  $\hat{t}_S$  as a fit parameter, then mark the time in the plot. We can see that for the quasar driven (type Q) subvolumes, all three fronts (inner, middle and outer) growth

stop at about 10 myear, on the same order of the life time of the quasar  $t_Q \sim 20$  myear and the fiducial recombination time  $t_S \sim 20$  myear. The deviation from free streaming indicates that by merely increasing the life span  $t_Q$  of the central quasar, we can not substantially increase the size of their CIR.

In S type type subvolumes, there is a similar tailing off for the inner fronts. However, the outer fronts continue their free streaming growth, behaving differently from the analytical model, which has stopped due to reaching the recombination time. We attribute this apparent excessive growth of the averaged S type outer front to the anisotropic growth via merging with other small ionized bubbles that are close to the CIR, as described later in the paper.

We note that our Monte-Carlo RT approach allows for superluminal growth of the CIR. This unphysical situation happens well before the first snapshot time which is 2 million years after the sources are turned on. The first snapshot, in which the Stromgren sphere typically has grown to about

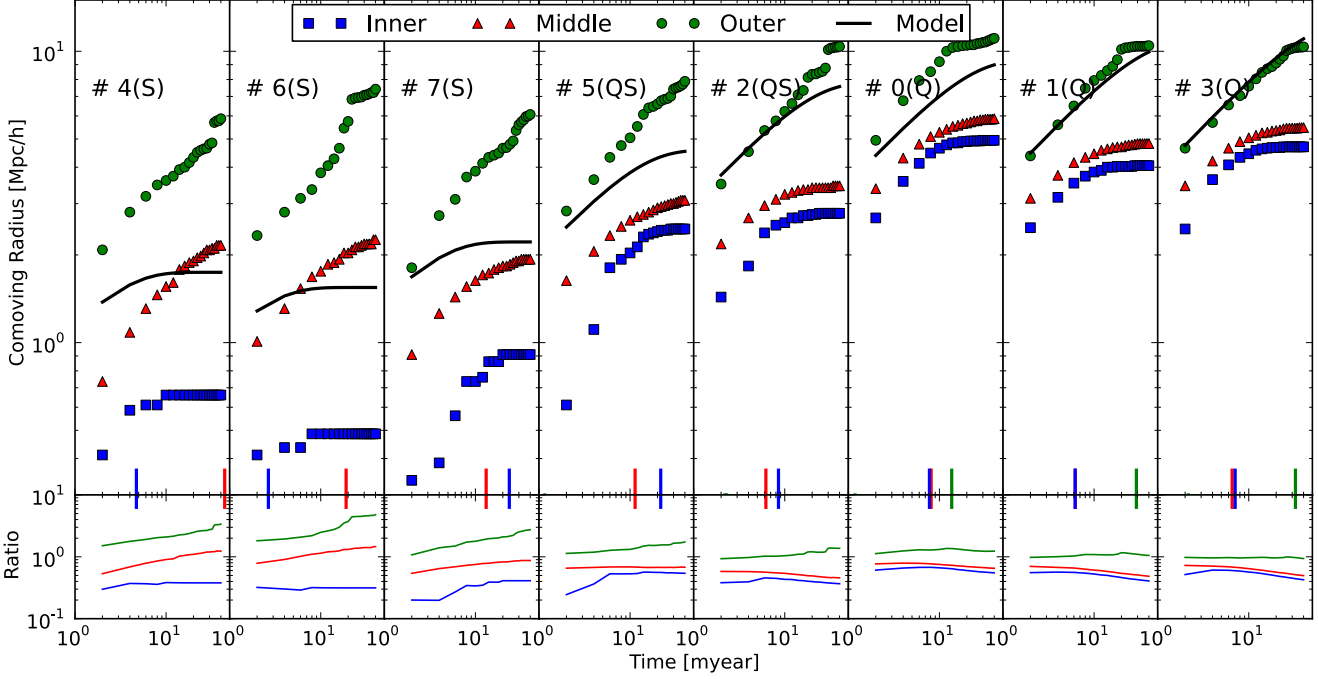


**Figure 8.** Evolution of three Quasar driven subvolumes. The top panels show the CIR radius as function of time; the thick black line is the fiducial analytic model as described in the text (equation 7). The vertical short lines show the recombination time in an analytic model as if it is fitted as a parameter to the simulation data points, which are marked with squares (Inner), triangles (Middle), and circles (Outer). The bottom panels show the ratio between the radius and the fiducial model.

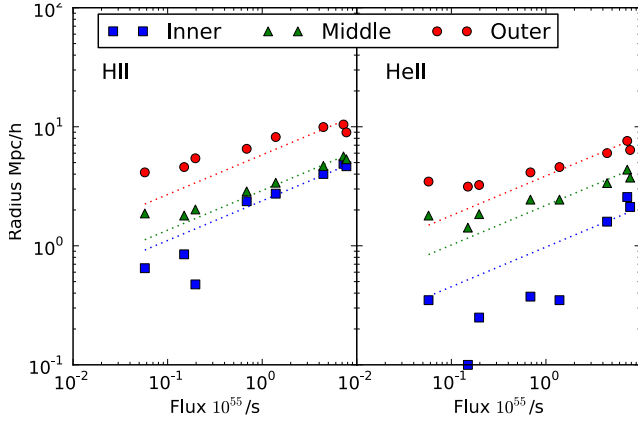


**Figure 6.** HII and HeIII CIR Front Radius. The left panel is for the HII CIRs, the right panel for the HeIII CIRs. The horizontal axis is the central source flux. The dotted line in the first two panels is fitting to the  $1/3$  free streaming power law.

10% of the full size, gives an upper bound to the contribution from superluminal growth. We conclude that the superluminal growth occurring at early time ( $< 2$  million years) and small radii ( $< 10\%$ ) does not play an important role in the final shape of the ionized bubble.

#### 6.4 MassiveBlack: Anisotropy of Ionized Regions

In Figure 9 we show the anisotropy measured using equation (13) of all 8 subvolumes. The anisotropy of different ionization fronts as a function of radius are marked with differ-

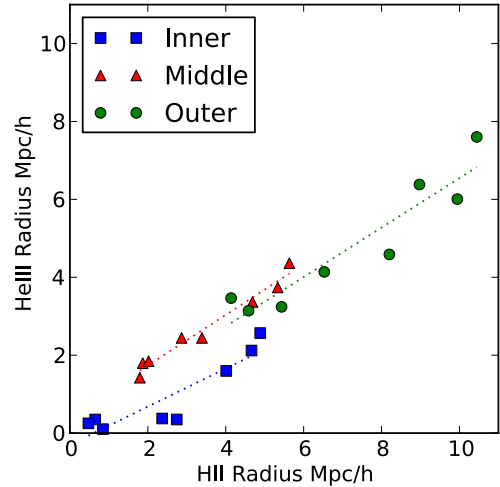


**Figure 7.** Correlation between HeIII CIR and HII CIR. HeIII CIRs is plotted against HII CIRs, and the linear regression for three fronts are shown with the dotted line.

ent symbols. As a reminder, in equation (13), the anisotropy  $A_s$  is the standard deviation of the ionization front radius, so that by comparing to the radius plotted on the x-axis it can be seen that the fronts are not very far from spherical symmetry ( $\sim 10\%$  variations). We find that larger ionized regions (corresponding to brighter quasar sources) are in general associated with more anisotropy.

In the simulation, the anisotropies of the inner and middle radii of the HII regions do not significantly depend on



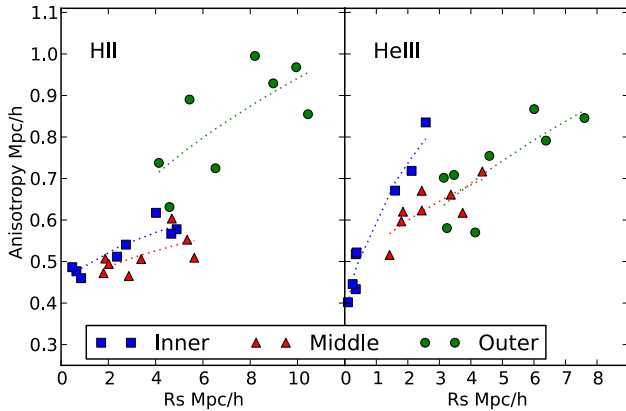


**Figure 9.** Anisotropy .vs. Radius. The left panel shows the anisotropy of three (inner, middle, outer) HII CIR fronts defined as in equation (13). The right panel shows the anisotropy of the HeIII fronts. The dotted lines are fits against a square-root + linear offset model and are only meant to guide the eye. All 8 subvolumes are displayed.

the radius (the curve is relatively flat), but the outer fronts have more anisotropy. The HeIII regions show a similar feature, except for the inner fronts of three type Q subvolumes, which have significantly stronger anisotropy.

These phenomena lead us to the following explanation, incorporating two contributing mechanisms:

(i) The anisotropic distribution of gas that attenuates the ionizing photons; when the density is high in a particular direction, the extra absorption decreases the radius of the ionized region in that direction.

(ii) The merging of nearby bubbles from clustered halos; when the density is sufficient to host bright sources lying in a certain direction, their extra photoionization increases the bubble radius in that direction. The outer front is more sensitive to merging than the inner and middle front.

For a small CIR (or a CIR in its early growing stage), no merging has occurred and only the density induced anisotropy is present. As the CIR grows, it overlaps with nearby ionized regions, resulting in the second type of anisotropy (due to overlapping). We note that this does not contradict the finding that clustering contributes to the smoothness of the extended ionization front, (due to Wyithe & Loeb (2007)), because after spherical averaging, the overall effect on the merged bubbles is to produce smoother ionization fronts.

In order to better visualize the structures which cause these anisotropies, we plot the distance to the different part of the ionization fronts in a Mollweide projection as seen from the point of view of the central source. These maps of the angularly dependent HII bubble radius,  $R_s$  are shown in Figure 10, where we plot the quasar driven subvolume 0 and stellar driven subvolume 4.

Looking from the top panels downwards for subvolume 0, we can first see clumps of mostly neutral gas close to the quasar which restrict the distance to the  $x_{\text{HI}} = 0.1$  fronts to be very close by ( $< 1 \text{ Mpc/h}$ ), compared to the mean distance for this neutral fraction of  $6 \text{ Mpc/h}$ . In the  $x_{\text{HI}} = 0.9$  plot, for subvolume 0 a prominent red region can be seen

at the top. This corresponds to a bubble which has merged with the central bubble. Next to each panel in Figure 10 we show a histogram of the  $R_s$  values. The secondary bubble is responsible for the small tail of high values region in  $x_{\text{HI}} = 0.9$  histogram, as well as giving an extra contribution to  $A_s$ .

Moving on to the stellar driven subvolume 4, right hand panels in Figure 10, we can see that the ionized region radius is smaller by approximately a factor of 3. Because this radius is small compared to the distance to nearby major halos, there is no sign of merging with other large bubbles, and the ionized region remains more isotropic. In the bottom panels of Figure 10 we show the Mollweide-projected mass density within the inscribed sphere of the subvolume. It is interesting to compare this clumpiness with the structure in the ionized bubble radius. We can see some correlation with some structures, but not as much as might be expected, indicating that the interaction of radiation with the clumpy medium surrounding the sources is a complex process.

In Figure 11, we show an orthogonal view to Figure 10, showing structure along rays moving out from the central source in some different directions. The outer HII front radii in three chosen directions are shown as a function of time. This allows us to see in detail how the clustering of halos affects the center bubble radius through merging as the simulation develops. The three directions are (i) one directed towards the second brightest source in the subvolume, (ii) one directed towards the merging bubble seen on the right hand side of Figure 5, and finally (iii) one oriented in a random direction not crossing any nearby secondary bubbles. In order to show the stronger bubble merging effect which would happen with more luminous sources, on the right hand side of Figure 11, we plot the same 3 sightlines, but after increasing the stellar luminosities by a factor of 10.

Merging happens as the central bubble touches the surrounding ones and meanwhile the radius along that direction significantly increases, compared to the radius without a nearby halo. This can be seen most clearly for sightline (iii) on the right in Figure 11. The development of the anisotropy due to merging of nearby ionized bubbles is responsible for the apparent rapid growth of the averaged outer Stromgren radius after the growth of the inner radius is stabilized for S type and QS type subvolumes. As the neutral fraction at the overlapping edge slowly drops below the threshold, two bubbles merge and the averaged radius increases. However, at the luminosities seen in the simulation (left hand panels of Figure 11), such merging mechanism is mostly limited in the growth of the outer front, for the slow growth of the pre-merging bubbles. It is also worth noting that in the absence of the effect of smoothing due to secondary ionization and the steep bubble edges will make the merging even more difficult to happen.

## 7 CONCLUSIONS

We have presented results from radiative transfer simulations in the vicinity of high redshift quasars in the Massive-Black simulation. We find that the rare brightest quasars drive a much more significant growth of ionized regions than in the purely stellar driven case. The ionized regions associated with active quasars are characterized by (i) a smooth ionized fraction transition from the middle to the outer

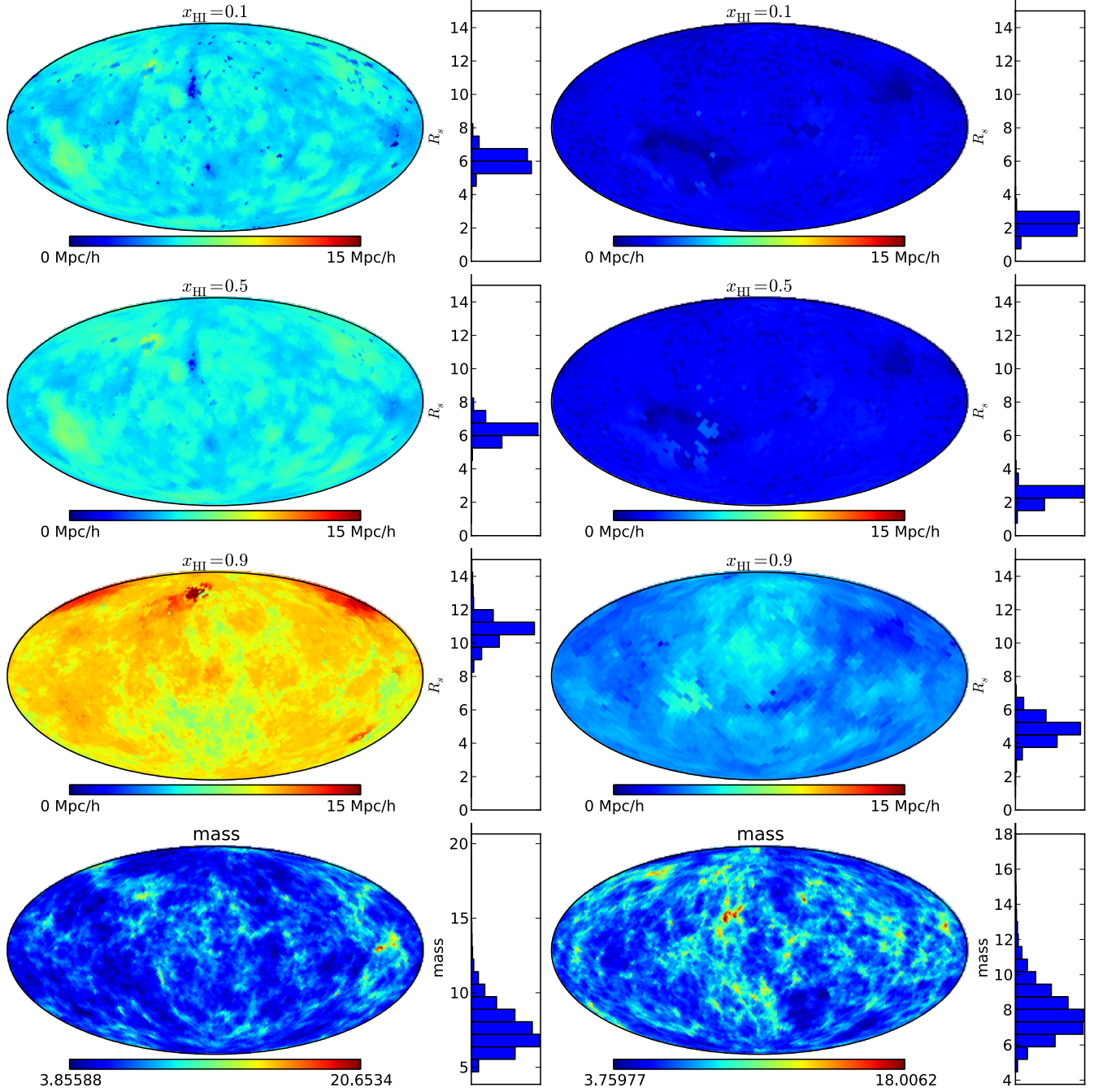


**Figure 10.** Angular Distribution of the HII Radius. The left column is subvolume 0(Q type) and the right column is subvolume 4(S type). From top to the bottom the inner ( $x_{\text{HII}}=0.1$ ), middle ( $x_{\text{HII}}=0.5$ ), and outer ( $x_{\text{HII}}=0.9$ ) fronts are shown. The histograms measure the variance of  $R_s$  in different angles, characterizing the anisotropy. The red region in the  $x_{\text{HII}} = 0.9$  plot of subvolume 0 is due to merging with a further away HII bubble. The less significant red in the center corresponds to the merging shown in Figure 5.

front, and (ii) an increased anisotropy in the front when it starts to overlap the nearby ionized regions. The nature of such growth is significantly more complex than a simple analytic growth of a single center bubble with clumping correction.

The largest HII bubble obtained in this simulation has a comoving radius of 10 Mpc/h, which is smaller than the general expectation that can fulfill the reionization of the universe.(Trac & Gnedin 2011; Wyithe & Loeb 2004; Ma-

jumdar et al. 2011) The quasar near zones we have presented in this paper are the primordial ancestors of the later much larger Stromgren spheres which will form near the end of the EoR. They are however relatively isolated regions that could be interesting objects for study in future 21cm surveys. After the  $z = 8$  epoch we have modelled in this paper, we expect that the global star formation in the MassiveBlack simulation increases significantly. This will eventually lead

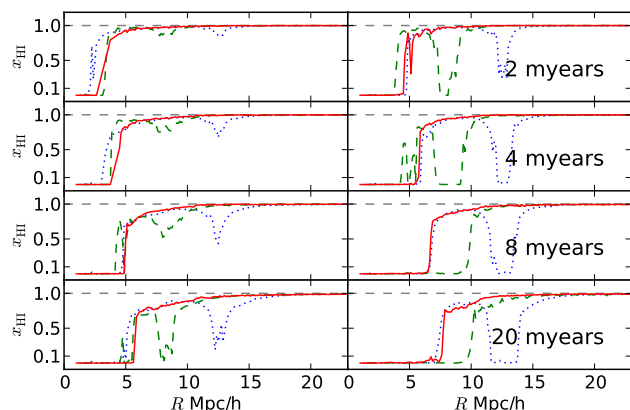


**Figure 11.** Time evolution of  $x_{\text{HI}}$ . Time evolution of  $x_{\text{HI}}$  in subvolume 0, along three selected sightlines: (i) the blue line is directed towards the second brighted halo in the subvolume; (ii) the green line is directed towards the merging bubble on the right shown in the slice plots; (iii) the red line is directed towards a random direction with no nearby bubbles. The left panel is the luminosity model used throughout the paper, while on the right the stellar luminosity is boosted by a factor of 10 to demonstrate a stronger merging effect.

to the global reionization of the universe. We plan to study this process and role of quasars in future work.

**Acknowledgements:** We acknowledge support from Moore foundation which enabled the radiative transfer simulations to be run at the McWilliams Center of Cosmology at Carnegie Mellon University. The MassiveBlack simulation was run on the Cray XT5 supercomputer Kraken at the National Institute for Computational Sciences. This research has been funded by the National Science Foundation (NSF) PetaApps program, OCI-0749212 and by NSF AST-1009781. The and visualizations were produced using Healpix (Górski et al. 2005), Healpy<sup>1</sup>, and Gaepsi<sup>2</sup> (Feng et al. 2011).

## References

Altay G., Croft R. A. C., Pelupessy I., 2008, *MNRAS*, 386, 1931 5  
 Bolton J. S., Haehnelt M. G., 2007, *MNRAS*, 382, 325 3  
 Bolton J. S., Haehnelt M. G., Warren S. J., Hewett P. C., Mortlock D. J., Venemans B. P., McMahon R. G., Simpson C., 2011, *MNRAS*, 416, L70 1  
 Cen R., Haiman Z., 2000, *ApJ*, 542, L75 4  
 Croft R. A. C., Altay G., 2008, *MNRAS*, 388, 1501 5  
 Croft R. A. C., Di Matteo T., Davé R., Hernquist L., Katz N., Fardal M. A., Weinberg D. H., 2001, *ApJ*, 557, 67 5  
 Datta K. K., Majumdar S., Bharadwaj S., Choudhury T. R., 2008, *MNRAS*, 391, 1900 1  
 DeGraf C., Di Matteo T., Khandai N., Croft R., Lopez J., Springel V., 2012, *MNRAS*, 424, 1892 2, 2  
 Di Matteo T., Colberg J., Springel V., Hernquist L., Sijacki D., 2008, *ApJ*, 676, 33 2

Di Matteo T., Khandai N., DeGraf C., Feng Y., Croft R. A. C., Lopez J., Springel V., 2012, *ApJ*, 745, L29 1, 2, 3  
 Fan X., Strauss M. A., Becker R. H., White R. L., Gunn J. E., Knapp G. R., Richards G. T., Schneider D. P., Brinkmann J., Fukugita M., 2006, *AJ*, 132, 117 3, 5.1  
 Feng Y., Croft R. A. C., Di Matteo T., Khandai N., Sargent R., Nourbakhsh I., Dille P., Bartley C., Springel V., Jana A., Gardner J., 2011, *ApJS*, 197, 18 7  
 Friedrich M. M., Mellema G., Iliev I. T., Shapiro P. R., 2012, *MNRAS*, p. 2385 6.3  
 Furlanetto S. R., Stoeber S. J., 2010, *MNRAS*, 404, 1869 5  
 Furlanetto S. R., Zaldarriaga M., Hernquist L., 2004, *ApJ*, 613, 1 3.2  
 Geil P. M., Wyithe J. S. B., 2008, *MNRAS*, 386, 1683 1  
 Giroux M. L., Shapiro P. R., 1996, *ApJS*, 102, 191 1  
 Górski K. M., Hivon E., Banday A. J., Wandelt B. D., Hansen F. K., Reinecke M., Bartelmann M., 2005, *ApJ*, 622, 759 7  
 Hopkins P. F., Richards G. T., Hernquist L., 2007, *ApJ*, 654, 731 3.1  
 Hui L., Gnedin N. Y., 1997, *MNRAS*, 292, 27 4, 5  
 Iliev I. T., Ciardi B., Alvarez M. A., Maselli A., Ferrara A., Gnedin N. Y., Mellema G., Nakamoto T., Norman M. L., Razoumov A. O., Rijkhorst E.-J., Ritzerveld J., Shapiro P. R., Susa H., Umemura M., Whalen D. J., 2006, *MNRAS*, 371, 1057 5.2  
 Khandai N., Feng Y., DeGraf C., Di Matteo T., Croft R. A. C., 2012, *MNRAS*, 423, 2397 2  
 Komatsu E., Dunkley J., Nolte M. R., Bennett C. L., Gold B., Hinshaw G., Jarosik N., Larson D., Limon M., Page L., Spergel D. N., Halpern M., Hill R. S., Kogut A., Meyer S. S., Tucker G. S., Weiland J. L., Wollack E., Wright E. L., 2009, *ApJS*, 180, 330 3  
 Loeb A., 2009, *J. Cosmology Astropart. Phys.*, 3, 22 1  
 Majumdar S., Choudhury T. R., Bharadwaj S., 2011, *ArXiv e-prints* 1, 4, 7  
 Maselli A., Ferrara A., Ciardi B., 2003, *MNRAS*, 345, 379 5  
 Mortlock D. J., Warren S. J., Venemans B. P., Patel M., Hewett P. C., McMahon R. G., Simpson C., Theuns T., González-Solares E. A., Adamson A., Dye S., Hambly N. C., Hirst P., Irwin M. J., Kuiper E., Lawrence A., Röttgering H. J. A., 2011, *Nature*, 474, 616 1  
 Pawlik A. H., Schaye J., van Scherpenzeel E., 2009, *MNRAS*, 394, 1812 4, 5  
 Shull J. M., van Steenberg M. E., 1985, *ApJ*, 298, 268 5  
 Sokasian A., Abel T., Hernquist L., Springel V., 2003, *MNRAS*, 344, 607 3.2  
 Springel V., Hernquist L., 2003, *MNRAS*, 339, 289 2, 2, 5  
 Srinivasan J. A., Wyithe J. S. B., 2007, *MNRAS*, 374, 627 1  
 Trac H. Y., Gnedin N. Y., 2011, *Advanced Science Letters*, 4, 228 1, 7  
 Willott C. J., Delorme P., Omont A., Bergeron J., Delfosse X., Forveille T., Albert L., Reylé C., Hill G. J., Gully-Santiago M., Vinten P., Crampton D., Hutchings J. B., Schade D., Simard L., Sawicki M., Beelen A., Cox P., 2007, *AJ*, 134, 2435 3  
 Wyithe J. S. B., Loeb A., 2004, *Nature*, 432, 194 1, 7  
 Wyithe J. S. B., Loeb A., 2007, *MNRAS*, 374, 960 6.3, 6.4

<sup>1</sup> <http://github.com/healpy/healpy>

<sup>2</sup> <https://github.com/rainwoodman/gaepsi>